JOURNAL OF CATALYSIS 116, 31–48 (1989)

Time Differential Perturbed Angular Correlation of γ-Rays Emitted from $^{99}Mo \rightarrow {}^{99}Tc$ in Molybdenum-Based Catalysts

The Nature of Molybdate Species in Molybdena/Alumina Catalysts

TILMAN BUTZ,* CLAUS VOGDT,†·‡ ANTON LERF,‡ AND HELMUT KNÖZINGER†

*Physik Department, Technische Universität München, 8046 Garching, Federal Republic of Germany; †Institut für Physikalische Chemie, Universität München, Sophienstrasse 11, 8000 München 2, Federal Republic of Germany; and ‡Walther-Meissner-Institut für Tieftemperaturforschung, Bayerische Akademie der Wissenschaften, 8046 Garching, Federal Republic of Germany

Received June 15, 1988; revised September 15, 1988

The time differential observation of the perturbed angular correlation of γ-rays emitted from radioactive $^{99}Mo \rightarrow {}^{99}Tc$ allows one to characterize different Mo species by their nuclear quadrupole interaction. An elementary introduction to this hyperfine spectroscopy is given together with examples of its application to crystalline Mo compounds, molybdate solutions at 77 and 300 K, and molybdates adsorbed on Al_2O_3 in the impregnated as well as in the dried and calcined state. It is shown that at sufficiently high solution concentrations, the heptamolybdate anion is adsorbed on the Al_2O_3 surface. Decondensation prior to adsorption can be excluded. The adsorbed heptamolybdate species are stable during the drying and calcination process. Postimpregnation of calcined Mo/Al_2O_3 catalysts with K_2CO_3 leads to decondensation, the extent of which depends on K_2CO_3 loading.

1. INTRODUCTION

Molybdenum-based catalysts are of great technological importance for hydrodesulfurization (*1*), hydrodenitrogenation (*2*), methanation (*3*), Fischer–Tropsch (*4*), and water gas shift (*5*) reactions. The active, usually sulfided form of the various catalysts develops under working conditions or is obtained by special treatments of the oxidic precursor. Many techniques have been applied to characterize the supported oxide on, e.g., Al_2O_3. Most of these techniques, however, cannot be readily applied to study the working catalyst *in situ*.

In this paper we present the application of a nuclear spectroscopy technique, namely "time differential perturbed angular correlations (TDPAC)." TDPAC probes essentially the same hyperfine interactions as nuclear magnetic resonance (NMR) or Mössbauer spectroscopy (ME). However, TDPAC turns out to be better suited to the present purpose for the following reasons: first, it can be applied at any temperature and pressure, under any atmosphere, including corrosive gases, and thus is ideally suited to *in situ* studies; second, a very small amount of radioactive labels, usually 10^9–10^{10} atoms, is sufficient, in contrast to the large number of nuclei required for NMR or ME; finally, crystalline as well as amorphous materials and even liquids can be studied, the latter being impossible by ME. The main disadvantage is, of course, that radioactive materials are to be used and a radiochemistry laboratory is required. Activities, however, are always low and in the 10–50 μCi range.

The principle of the application of TDPAC to Mo compounds and Mo-based catalysts is as follows: one determines the interaction between the nuclear quadrupole moment and the electric field gradient (EFG) produced by all extranuclear charges. For Mo atoms in a perfect octahedral or tetrahedral environment the EFG vanishes due to symmetry. Hence, there is

0021-9517/89 $3.00

no nuclear quadrupole interaction (NQI). A simple condensation of polyhedra leads to a distortion of the polyhedra and, hence, to a nonzero NQI. This is characteristic for each compound and can be used as a fingerprint. Actually the EFG is a second rank tensor and hence also contains information about the symmetry of the environment of the probe atom. Unfortunately, the theory of NQIs in compounds, as well as in pure elements, is not sufficiently accurate at present to offer much help in the interpretation of data. An important observation is that the NQI in nonionic compounds appears to be governed by the nearest neighbor environment. Hence, crystalline and amorphous molybdates with about the same local order yield very similar spectra.

In this paper we shall first give an elementary description of the theory of TDPAC as it is relevant for the present purpose, followed by a short description of the experimental setup and the data reduction. We give examples for crystalline Mo compounds, liquid and frozen molybdate solutions, and finally molybdates adsorbed onto Al_2O_3 in the impregnated, dried, and calcined state. For the latter studies we shall classify the Mo species into isolated Mo–O polyhedra and condensed Mo–O polyhedra sharing edges. The fraction of condensed Mo–O polyhedra is found to be large in all preparation steps ($\geq$75%) and the spectra all resemble closely that of the heptamolybdate. An efficient decondensation of Mo–O polyhedra can be accomplished by postimpregnation with K_2CO_3.

2. TDPAC—THEORY, SETUP, DATA REDUCTION

2.1. Physical Background and Theory [6–8]

The basic principle of TDPAC relies on the fact that a nucleus being in an unstable excited state will decay via the emission of a particle, frequently a γ-quantum, whose emission probability depends on the orientation of the nuclear spin. The reason for this correlation between the emission direction and the spin orientation is based on the concept of conservation of angular momentum: the vectors describing the magnitude and orientation of the spins before and after the emission of the γ-quantum and the vector describing the direction of emission and the magnitude of the angular momentum carried away by the γ-quantum (at least one unit of $\hbar$) must add up to zero or "form a triangle." In an ensemble of radioactive nuclei usually the spin orientations are distributed randomly. Hence, a radioactive sample will emit γ-quanta isotropically, as shown in Fig. 1a. In contrast, the emission would be anisotropic provided that the nuclear spins were oriented. This can be accomplished, e.g., by orienting the nuclei in a strong magnetic field at temperatures of the order of 1 mK. The angular distribution of emission of an ensemble of oriented nuclei would then look similar to that shown in Fig. 1b and can be written as

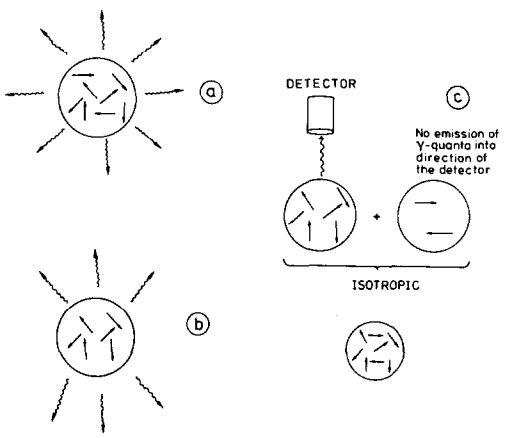

FIG. 1. (a) Isotropic emission of γ-quanta from nuclei with randomly oriented spins. (b) Anisotropic emission of γ-quanta from oriented nuclei. (c) By observation of a γ-quantum in a certain direction, a subensemble of nuclei is selected which possesses an alignment.

$$W(\vartheta) = 1 + B_2P_2(\cos\vartheta) + B_4P_4(\cos\vartheta) + \cdots. \quad (1)$$

Here, ϑ denotes the angle between the direction of emission and the quantization axis, the coefficients B_k describe the degree

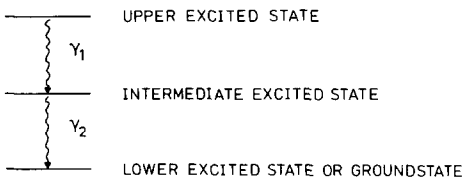

FIG. 2. γ–γ-cascade used in TDPAC experiments.

of orientation, and the $P_k(\cos \vartheta)$ are Legendre polynomials. Usually the term with $k = 2$ is sufficient. Because of parity conservation of the electromagnetic interaction only *even* terms appear in Eq. (1); i.e., there is no forward–backward asymmetry.

Instead of using oriented nuclei one could profit from the fact that the mere observation of a γ-quantum in a given direction selects a subensemble of randomly oriented spins; not all nuclei would emit γ-quanta in this direction, only those which happen to have the proper spin orientation. This situation is sketched in Fig. 1c.

Now, if these nuclei would emit another γ-quantum, say γ_2, the subensemble shown in Fig. 1c would do so in an anisotropic manner because it possesses a certain degree of orientation. This type of orientation is called alignment because states with quantum numbers $+m$ and $-m$ have the same population. Hence, it is necessary to measure the angular distribution of γ_2 in *coincidence* with the preceding γ_1 in order to ensure that they come from the same nucleus. In other words, the emission of γ_2 is correlated with the emission of γ_1. Thus the heart of any γ–γ-angular correlation measurement is a nucleus in an excited state which emits two γ-quanta successively or in a "cascade" as shown in Fig. 2.

The experimental setup is shown schematically in Fig. 3 and the correlation between the two γ-quanta from an ensemble of nuclei can be written as follows, in close analogy to Eq. (1):

$$W(\theta) = 1 + A_2 P_2(\cos \theta) + \cdots . \quad (2)$$

Here, $W(\theta)$ is the coincidence count rate, A_2 describes the degree of angular correlation between the two γ-quanta, and θ is the angle between the emission directions of γ_1 and γ_2. A_2 depends entirely on nuclear properties of the cascade, i.e., the nuclear spins involved and the multipolarities of the transitions (i.e., dipole, quadrupole). It is frequently called the "anisotropy" and is a constant. Usually, the term A_2 is sufficient. The coincidence count rate as a function of angle θ between the two γ-quanta looks like that shown in Fig. 4.

It can happen that the lifetime of the intermediate excited state is long compared to the instrumental time resolution of the coincidence circuit. We could then perform a time differential measurement, i.e., count coincidences between γ_1 and γ_2 as a function of delay time between γ_1 and γ_2. The

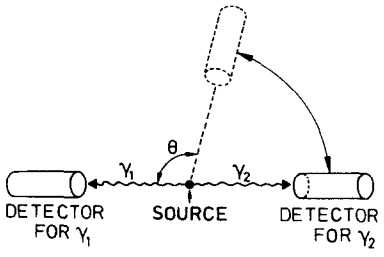

FIG. 3. Schematic experimental setup showing a fixed detector for γ_1 and a movable detector for γ_2. By measurement of the coincidence count rate vs the angle θ between detectors, the anisotropy A_2 of the angular correlation is obtained.

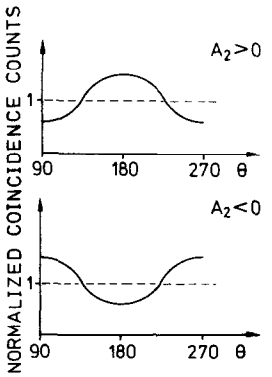

FIG. 4. Normalized coincidence count rate vs angle θ between detectors for positive anisotropy (top) and for negative anisotropy (bottom).

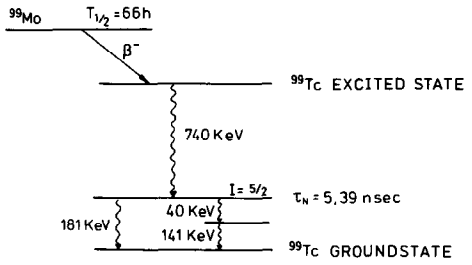

FIG. 5. Simplified decay scheme of ^{99}Mo. Because the $I = \frac{5}{2}$ level is deexcited via two routes, two cascades can be measured simultaneously: the 740–181 keV cascade and the triple cascade 740–40–141 keV.

time differential angular correlation would then read

$$W(\theta, t) \sim \exp(-t/\tau_N)[1 + A_2P_2(\cos\theta) + \cdots] \quad (3)$$

with τ_N being the lifetime of the intermediate state. This equation, however, holds true only if the angular correlation is not perturbed by any extranuclear fields during the lifetime τ_N. In general, the extranuclear fields, either magnetic fields or inhomogeneous electric fields, would interact with the nuclear magnetic dipole or the electric quadrupole moment, respectively, and turn the spin orientation while the nucleus is in the intermediate state. This torque leads to a spin precession, and the resulting perturbation of the angular correlation can now be written as

$$W(\theta, t) \sim \exp(-t/\tau_N)[1 + A_2G_2(t)P_2(\cos\theta) + \cdots] \quad (4)$$

where $G_2(t)$, the perturbation function, contains all relevant information characterizing the fate of the nucleus while it is in the intermediate state.

Before giving examples for relevant perturbation functions we quote the cascade of interest in the present study. Figure 5 shows a simplified decay scheme of ^{99}Mo ($T_{1/2}$ = 66 h) (*9*). Only the two cascades which have been used in the present study are shown. One cascade is actually a triple cascade where the intermediate 40 keV γ-quantum remains unobserved. This does not yield any complications and is incorporated in the anisotropy A_2. The 740–181 keV cascade has a positive anisotropy, $A_2 \approx +10\%$, whereas the 740–(40)–141 keV cascade has a negative anisotropy, $A_2 \approx -11\%$. (These numbers are derived from TDPAC experiments and deviate from values reported by others (*10*) which were based on unperturbed time integral measurements.) Both cascades can be used for the study of the interaction of the $I = \frac{5}{2}$ nuclear state. The latter cascade yields a slightly higher anisotropy and a slightly higher coincidence count rate. However, with our detectors we could not avoid the rather strong admixture of the 142 keV line from ^{99m}Tc ($T_{1/2}$ = 6 h) to the 141 keV line and we thus have a much larger background of accidental coincidences for this cascade than for the 740–181 keV cascade.

The intermediate spin $\frac{5}{2}$ state has a nonzero but unknown nuclear quadrupole moment. If placed in an inhomogeneous electric field, this nonspherical nucleus can have certain orientations with respect to the gradient of the electric field which differ in energy (much like the parallel and antiparallel orientation of a magnetic dipole in a magnetic field). A quantum mechanical treatment yields the energies

$$E_m = 3e^2qQm^2/4I(2I - 1), \quad m = -I, -I + 1, \ldots, I - 1, I. \quad (5)$$

eQ denotes the nuclear quadrupole moment; eq is the largest component of the EFG tensor, which is assumed here to be axially symmetric (i.e., $eq = V_{zz}$, $V_{xx} = V_{yy}$); and I is the nuclear spin, with m being a quantum number to label the possible orientations. For the present case the intermediate state with $I = \frac{5}{2}$ will split into three substates differing in energy by

$$E_{m,m'} = E_m - E_{m'} = 3e^2qQ(m^2 - m'^2)/40.$$

Hence, (i) for $m = \pm 3/2$ and $m' = \pm 1/2$;

$$E_{\pm 3/2,\pm 1/2} = 6e^2qQ/40; \quad (6)$$

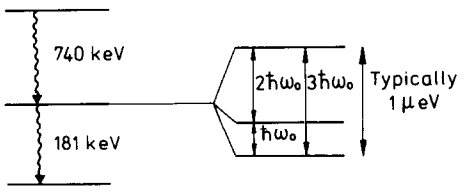

FIG. 6. Quadrupole splitting of the $I = \frac{5}{2}$ intermediate state (assuming axial symmetry).

(ii) for $m = \pm 5/2$ and $m' = \pm 3/2$;

$$E_{\pm 5/2,\pm 3/2} = 12e^2qQ/40;$$

(iii) for $m = \pm 5/2$ and $m' = \pm 1/2$;

$$E_{\pm 5/2,\pm 1/2} = 18e^2qQ/40.$$

With the definition $\omega_0 = 6e^2qQ/40\hbar$ (we have disregarded the sign of ω_0 which cannot be determined in a γ–γ-correlation experiment anyway), we have the picture shown in Fig. 6. Now, in analogy to the Larmor precession we can think of a precession of the nuclear spin with frequencies $\omega_n = n\omega_0$ with $n = 1, 2$, and 3. (This analogy is very fruitful conceptually but not entirely rigorous.)

The EFG is a traceless tensor ($V_{xx} + V_{yy} + V_{zz} = 0$) and can have axial symmetry or not. In the principal axis coordinate system we have

$$\begin{pmatrix} V_{xx} & 0 & 0 \\ 0 & V_{yy} & 0 \\ 0 & 0 & V_{zz} \end{pmatrix}. \tag{7}$$

If we rearrange the components such that $|V_{zz}| \geq |V_{xx}| \geq |V_{yy}|$ we can define the asymmetry parameter η as

$$\eta = \left| \frac{V_{xx} - V_{yy}}{V_{zz}} \right|. \tag{8}$$

If $V_{xx} = V_{yy}$ we have $\eta = 0$ or axial symmetry; otherwise we have $0 < \eta \leq 1$. A deviation from axial symmetry modifies the level splitting shown in Fig. 6 and consequently the precession frequencies. In general this no longer leads to a periodic precession pattern because the frequency ratios now differ from the simple 1 : 2 : 3 ratio.

We now give some typical examples for the perturbation function $G_2(t)$ for $I = \frac{5}{2}$, pure NQI, and random powder samples (in contrast to single crystals or textured powders). In addition to the perturbation function $G_2(t)$ we also show its Fourier transform.

The simplest case, the absence of any NQI, is shown in Fig. 7a. In this case $G_2(t) = 1$ and the Fourier transform is just a peak centered at zero frequency with the instrumental width determined by the width of

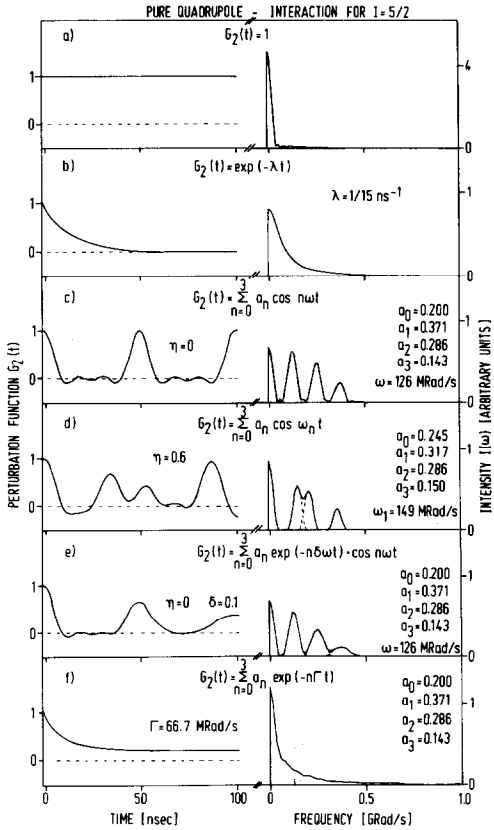

FIG. 7. Perturbation functions (left) and their Fourier transforms (right) for $I = \frac{5}{2}$ and pure quadrupole interaction: (a) unperturbed case; (b) fast relaxation case typical for liquids; (c) static, axially symmetric NQI; (d) static, nonaxially symmetric NQI; (e) static, axially symmetric NQI with a finite frequency distribution leading to damping in the time spectra or line broadening in the Fourier spectra; (f) static NQI with a distribution of frequencies (half-width at half-maximum) centered around a mean zero frequency.

the time window over which $G_2(t)$ is observable.

The next case deals with fast relaxation. For a spherical rotor and an isotropic motion we have a simple exponential decay: $G_2(t) = \exp(-\lambda_2 t)$ with $\lambda_2 = 2.8\langle\omega^2\rangle\tau_c$. Here, $\langle\omega^2\rangle$ denotes the time-averaged NQI and τ_c is the reorientational correlation time. The Fourier transform now is a Lorentzian convoluted with the instrumental resolution. This fast relaxation case is shown in Fig. 7b.

The third case is the time-independent (static) NQI. Figure 7c shows two periods of $G_2(t) = 0.2 + 0.371\cos(\omega_0 t) + 0.286\cos(2\omega_0 t) + 0.143\cos(3\omega_0 t)$. Here, axial symmetry was assumed. The Fourier transform consists of a peak centered at zero frequency with intensity 0.2 and three other peaks centered at ω_0, $2\omega_0$, and $3\omega_0$ with intensities 0.371, 0.286, and 0.143, respectively. The time-independent term with intensity 0.2 is a purely quantum mechanical effect and results from "interference" of a sublevel with "itself" (i.e., $m = m'$).

Figure 7d shows the beginning of $G_2(t)$ for a nonaxially symmetric case ($\eta = 0.6$). Now the Fourier peaks are no longer equidistant and have modified intensities. Note, however, that the sum rule still applies: $\omega_3 = \omega_1 + \omega_2$.

Another case of interest is the effect of a finite distribution of interaction frequencies due to small site inequivalencies. This introduces a time-dependent reduction of the oscillation amplitudes, i.e., "damping" in the time spectra or "line broadening" in the Fourier spectra. This is shown in Fig. 7e for a Lorentzian distribution of frequencies with half-width $\delta\omega_0/\omega_0$.

A special case, the distribution around zero frequency is displayed in Fig. 7f (Lorentzian with half-width Γ). Note that the anisotropy does not fall to zero as in the case of fast relaxation but stays constant at the "hardcore" value of 0.2. Finally, it should be mentioned that a spectrum can consist of several components, e.g., two static patterns of the type of Fig. 7c with two different frequencies. The relative intensities would then immediately allow the quantitative identification of two different species. Since the total anisotropy A_2 is constant and known, the sum of all individual contributions must be constant; there is in principle no way to miss the contribution from a certain species due to technical problems.

In practice, the finite resolving time of the coincidence apparatus further modifies the spectra. As a rough estimate of the effect of the finite time resolution we can use the approximate amplitude reduction factor $f_n = \exp(-0.09\,\omega_n^2\tau_R^2)$ with τ_R denoting the width of the time resolution function (full width at half-maximum). Note that the higher frequency components are progressively more suppressed but that no damping or line broadening is introduced by the finite resolving time.

2.2. *Experimental Setup (8)*

The TDPAC setup used in the present work consists of four detectors in a plane as sketched in Fig. 8. Each γ-detector consists of a NaI(Tl) scintillation crystal (1.75 × 2-in. diameter) mounted on RCA8850 photomultipliers. There are two separate circuits; in the slow circuit the signals are analyzed with respect to the γ-energy and the coincidences of proper pulses from two detectors are established, essentially without any time resolution. Table 1 shows the 12 possible combinations of detectors, of which 8 are used in the present experiment. The fast circuit treats each incoming pulse irrespec-

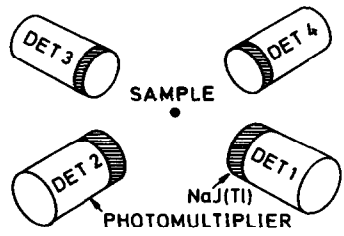

FIG. 8. Schematic of the arrangement of four detectors in a plane being 90° apart from each other.

TABLE 1

Summary of All 12 Possible Detector Combinations in a Four-Detector Arrangement[a]

Subgroup number	γ_1 detected by detector number	γ_2 detected by detector number	θ (°)
1	1	3	180
2	3	1	180
3	2	4	180
4	4	2	180
5	3	2	90
6	2	3	90
7	1	4	90
8	4	1	90
9	1	2	90
10	2	1	90
11	3	4	90
12	4	3	90

[a] The first eight combinations were used in the present experiments.

tive of its energy and is used for timing purposes. A constant fraction trigger provides fast logic signals which are fed to a time-to-pulse height converter, the output of which is then gated and routed into the 8 different subgroups of a multichannel analyzer. Thus we record 8 coincidence spectra simultaneously. Each subgroup contains a spectrum of the type shown in Fig. 9. Apart from a constant background from accidental coincidences, i.e., the energy and time conditions were by chance fulfilled by two nuclei decaying practically simultaneously, there is the exponentially decaying curve of true coincidences onto which the spin precession signal ($= G_2(t)$) is superimposed. The exponential decay is to the right side when the start detector records γ_1 and it is to the left side when it records γ_2. The initial time, t_0, is placed in the middle of the subgroup by a suitable delay in the stop channel.

2.3. *Data Reduction* (8)

The data reduction proceeds in the following way. First, the accidental background is substracted from each subgroup. In order to estimate this background we used that part of the spectra which does not contain true coincidences at all, i.e., the region for "negative times" (left half in Fig. 9). Next, we invert the spectra which decay to the left side such that all spectra decay to the right side. Then all spectra are shifted to a common time origin. This t_0 for each subgroup had been previously determined by measuring prompt coincidences, e.g., from a ^{60}Co source. This method of t_0 determination allows deduction of both the center position and the resolution time τ_R. We now form the ratio

$$R = A_2G_2(t) = 2\,\frac{\sqrt[4]{W_{13}W_{31}W_{24}W_{42}} - \sqrt[4]{W_{14}W_{41}W_{23}W_{32}}}{\sqrt[4]{W_{13}W_{31}W_{24}W_{42}} + 2\sqrt[4]{W_{14}W_{41}W_{23}W_{32}}}. \quad (9)$$

W_{ij} denote the coincidence count rates (already corrected for accidental background) between detector i (accepting γ_1) and detector j (accepting γ_2). Inserting Eq. (4) shows that this ratio equals $A_2G_2(t)$. The exponential decay factors cancel. Moreover, the detector efficiencies cancel as well because each detector appears once for each γ-energy both in the numerator and in the denominator. In many cases data were obtained for both cascades simultaneously and were then combined. Since A_2(740–181) is positive, whereas A_2(740–40–141) is negative, we form a weighted difference: wR(740–181) $-$ $(1 - w)R$(740–40–141). Here, w is proportional to the statistical ac-

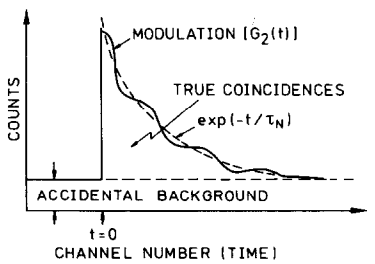

FIG. 9. Content of a subgroup in the multichannel analyzer (schematic).

curacy at each data point (for details see Ref. (*11*)).

It is the above ratio (Eq. (9)) which is shown in subsequent figures. The calculation of statistical errors for each data point is straightforward. Because there are fewer true coincidences at later times, the statistical accuracy decreases with increasing delay time between γ_1 and γ_2.

In practically all cases computer fits of appropriate theoretical functions of the types shown in Fig. 8 were performed. In this procedure, the complete analytical expressions for the effect of the finite time resolution were used as described in Ref. (*12*).

In some cases we performed Fourier transforms of the reduced data according to Eq. (9). Here we used a Kaiser–Bessel window function (a suitable compromise between side-lobe suppression and deterioration of frequency resolution was obtained with a parameter 4 rather than the maximum allowed 9 (*13*)). The data were implemented by a suitable number of zeros (so-called zero-padding) so as to reduce truncation effects and guarantee the 2^N number of data required for the fast Fourier transform routines.

3. EXAMPLES

3.1. Crystalline Compounds

Molybdenum metal. The simplest example to start with is Mo metal. Due to its cubic structure the EFG is zero and the unperturbed anisotropy should be observed. This is indeed the case, as shown in Fig. 10 for the 740–40–141 keV cascade.[1] A least-squares fit assuming a discrete frequency yields the very low value of $\omega = 10(3)$ Mrad/s (*14*). This could be due to impurities or extended defects in the sample. This measurement yields an accurate value for the anisotropy: $A_2 = -8.5\%$. When corrected for solid angle correction factors we obtain $A_2^{\text{corr}} = -10.2\%$. Mo metal was neutron irradiated and measured as irradiated because we do not expect to produce radiation damage (if it occurs it anneals even at room temperature). As discussed in Ref. (*8*) aftereffects due to the preceding β-decay are not expected because the metallic environment allows for a very rapid rearrangement of the electronic shell after the nuclear transmutation. In fact, for all systems studied thus far we have never had any indication of aftereffects.

Compounds with isolated Mo–O/S tetrahedra. The following compounds with isolated Mo–O/S tetrahedra at room temperature were investigated (*14*): $Fe_2(MoO_4)_3$, $Al_2(MoO_4)_3$, and $(NH_4)_2MoS_4$. The first two were measured as irradiated; the third was dissolved in water after irradiation and precipitated with butanol/acetone. A typical spectrum for $Fe_2(MoO_4)_3$ is shown in Fig. 10. In this, as well as in the other two cases, there is a very slow decrease of the anisotropy which can be fitted well by a frequency distribution around a mean frequency $\omega = 0$. The half-width of this distribution was $\Gamma = 45(4)$, 93(21), and 53(9) Mrad/s for $Fe_2(MoO_4)_3$, $Al_2(MoO_4)_3$, and $(NH_4)_2MoS_4$, respectively (Fig. 10). A fit with a low but finite frequency was not successful. In the first two cases, the broadening could arise from radiation defects or other sample imperfections. The thiomolybdate, however, was dissolved in water and precipitated after irradiation. In this case, all radiation damage, which was clearly observed for a sample measured as irradiated, is removed. The origin of the broadening is not clear in this case. It could arise from imperfections introduced during the precipitation. Moreover, we required a minority fraction of about 7% with $\omega_1' = 472(36)$ Mrad/s to account for the structure superimposed onto the slow decay. This is certainly due to imperfections introduced during precipitation. In any case, the NQI in compounds with isolated Mo–O/S tetrahedra turned out to be zero or very small. Since the NQI vanishes for ideal tetrahe-

[1] The measurement was performed at 77 K for technical reasons. Room temperature data would be identical.

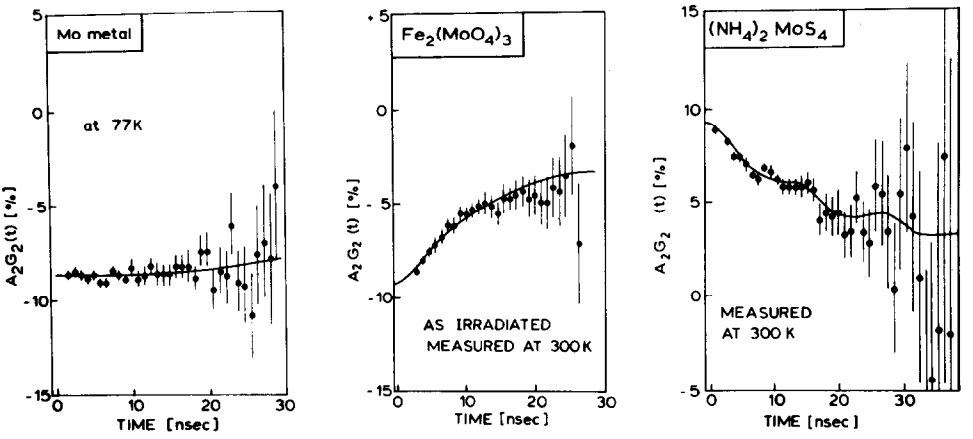

FIG. 10. TDPAC spectra of Mo metal (740–40–141 keV cascade only) taken at 77 K; $Fe_2(MoO_4)_3$ (740–40–141 keV cascade only) taken at 300 K; and $(NH_4)_2MoS_4$ (both cascades simultaneously) taken at 300 K.

dral coordination due to symmetry, we conclude that the tetrahedra in these compounds are virtually undistorted.

Compounds with condensed Mo–O/S polyhedra. The following compounds with condensed Mo–O/S polyhedra were studied at room temperature, except where stated otherwise: MoO_2, MoO_3, $(NH_4)_6Mo_7O_{24} \cdot 2H_2O$ (APM), the intercalation compound $Na_{0.5}(H_2O)_yMoO_3$ (*14*), the trigonal prismatic-layered compound MoS_2, and amorphous MoS_3 (*14, 15*). MoO_3 turns deep blue upon irradiation (*15*) due to a high *defect* density, as indicated in the TDPAC spectra by a high-frequency component around 0.5 Grad/s (Fig. 11a). This material was sublimed at 720°C after irradiation. The TDPAC spectrum for the sublimed material no longer exhibits the high-frequency component attributed to radiation-induced defects (Fig. 11b). Similarly, solid APM turns dark brown upon irradiation and when dissolved in water, gives a deep blue solution, as reported earlier (*16*). Interestingly, the solution remains blue for several hours, showing the extreme stability of the color center formed, which gives rise to a high-frequency component at 800 Mrad/s in the TDPAC spectrum. We believe that this center consists of an oxygen vacancy in the coordination shell of that central Mo atom which has no terminal oxygens; the reasoning is as follows: (i) very similar high-frequency components in the gigaradians per second range are observed for irradiated MoO_3 and APM (*15*); (ii) sixfold coordinated Mo(V) in Mo-EDTA (*11*) and in $Na_{0.5}(H_2O)_yMoO_3$ (*14*) exhibits frequencies around 300 Mrad/s only. Therefore, at least for neutron irradiations, the oxygen vacancy model for the color center in APM is strongly favored over the model assuming a reduced APM via radiolysis (*16*). After stirring the solution in air until colorless we precipitated APM with ethanol. The resulting spectrum is shown in Fig. 17, bottom.

The case of APM poses some problems

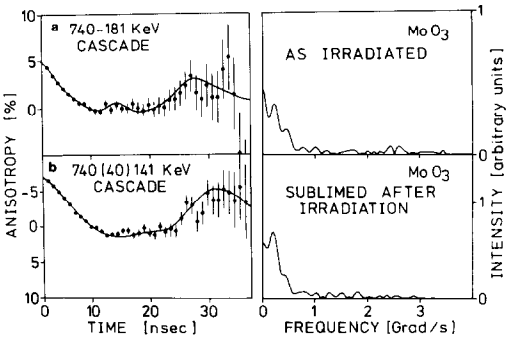

FIG. 11. TDPAC and Fourier spectra of MoO_3 at 300 K. (a) Taken as irradiated; (b) taken after sublimation in order to remove radiation defects.

TABLE 2

Summary of NQI Parameters for Various Crystalline Molybdenum Compounds

Compound	Temp (K)	ω_1 (Mrad/s)	$\delta\omega_1$ (HWHM) (Mrad/s)	η	α (%)	ω_1' (Mrad/s)	$\delta\omega_1'$ (HWHM) (Mrad/s)	η'
$Fe_2(MoO_4)_3$	300	0	45(4)	0[a]	100	—	—	—
$Al_2(MoO_4)_3$	300	0	93(21)	0[a]	100	—	—	—
MoO_2	300	73(2)	18(5)	0[a]	100	—	—	—
MoO_3	300	175(4)	0	0.55(5)	100	—	—	—
$Na_{0.5}(H_2O)_4MoO_3$	77	294(11)	0	0.41(6)	100	—	—	—
$(NH_4)_6Mo_7O_{24} \cdot 2H_2O$	300	181(3)	0	0.46(3)	76(2)	416(10)	0	0.29(5)
		or 212(5)	0	0.49[a]	59(3)	324(13)	0	0.59(5)
MoS_2	300	112(2)	0	0	100	—	—	—
$(NH_4)_2MoS_4$	300	0	31(3)	0[a]	93(2)	472(36)	0	1[a]
$(NH_4)_2Mo_3S_{13}$	300	314(5)	0	0.58(3)	60(3)	165(5)	0	0

[a] Assumed value.

in the data analysis. Since there are seven inequivalent Mo atoms per molecule we should in principle expect seven different NQIs. This would be much beyond the capabilities of the least-squares analysis due to the limitation of the data. A fairly satisfactory fit to the data points could be achieved assuming a single Mo site with a small distribution in frequency. We thus obtained $\omega = 230(5)$ Mrad/s and $\eta = 0.26(3)$. The width of the frequency distribution was 16(9) Mrad/s (half-width at half-maximum). However, very accurate measurements obtained by summing up several spectra obtained for several separate samples revealed that the intensities of the observed peaks (fundamental and harmonics) do not agree well with those of the adjusted theoretical spectrum. An analysis with two inequivalent Mo sites yielded two possibilities: (a) $\omega_1 = 181(3)$ Mrad/s and $\eta = 0.46(3)$ for the majority site (mole fraction 76(2)%) and $\omega_1' = 416(10)$ Mrad/s and $\eta' = 0.29(5)$ for the minority site; (b) $\omega_1 = 212(5)$ Mrad/s and $\eta = 0.49$ for the majority site (mole fraction 59(3)%) and $\omega_1' = 324(13)$ Mrad/s and $\eta' = 0.59(3)$ for the minority site. In the second case, we could tentatively assign the minority site to the central group of three Mo–O octahedra. The majority would then be assigned to the other four Mo–O octahedra which have terminal oxygen atoms. Since both ways to analyze the data produce very similar theoretical spectra, at least in the limited observable time range of about 35 ns, we preferred to restrict ourselves to the simple single-site analysis for all subsequent applications.

The results of Table 2 show that all compounds with isolated Mo–O/S tetrahedra exhibit a vanishing or very low NQI, whereas the compounds with condensed polyhedra have interaction frequencies in the range from 75 to about 300 Mrad/s. It is not clear whether the almost linear increase of the average NQI with increasing O/Mo ratio (and to a lesser extent with the S/Mo ratio) has any significance. It appears that the Mo(VI) compounds have systematically higher NQIs than the Mo(IV) compounds. Large NQIs are expected for Mo(V), since the quadrupolar polarizability for ions with a single electron outside the closed shell core is particularly large. This is very clearly shown by recent comparative studies of Mo(VI)-EDTA and Mo(V)-EDTA (*11*).

3.2. APM Solutions

A very simple example of a TDPAC spectrum of a liquid is shown in Fig. 12 for APM dissolved in H_2O at pH 5.5 and room

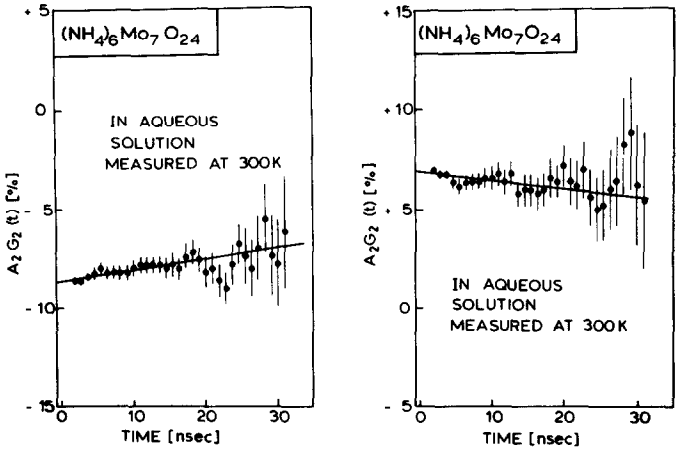

FIG. 12. TDPAC spectra of APM dissolved in water at pH 5.5 taken at room temperature (left, 740–40–141 keV cascade; right, 740–181 keV cascade).

temperature (left, 740–40–141 keV cascade; right, 740–181 keV cascade). At $t = 0$ we find $A_2 = -10.5\%$ and $A_2 = +9\%$, respectively, already corrected for solid angle correction factors (about 20%). Both values are in disagreement with the values quoted by Singh and Sahota (*10*). The 181 and 141 keV lines were well separated in our experiments. Therefore the admixtures of either of the unwanted lines in the cascade, which would reduce the observed anisotropies, can be ruled out as a possible source for this discrepancy. The anisotropy decreases very slightly with time, and a least-squares fit of an exponential decay, appropriate for a spherical rotor and rapid isotropic tumbling motion of the molecule, yielded a decay constant of $\lambda_2 = 1/142(18)$ ns^{-1} and $\lambda_2 = 1/134(32)$ ns^{-1} for the 740–40–141 keV and the 740–181 keV cascades, respectively (*14*).

At pH 5.5 we have heptamolybdate anions in solution, as can be easily verified by measuring the frozen solution (see below). Assuming an average NQI of $\omega = 230$ Mrad/s and neglecting the deviation from axial symmetry, we obtain from $\lambda_2 = 2.8\langle\omega^2\rangle\tau_c$ a reorientational correlation time $\tau_c = 48$ ps. From the volume V of the tumbling species can be derived via the Debye formula:

$$\tau_c = \frac{\eta_0 \cdot V}{k_B T}. \tag{10}$$

In Eq. (10), η_0 denotes the viscosity. Taking $\eta_0 = 1$ cP we obtain an average volume of about 6×10^{-3} nm^3. Hence, the heptamolybdate ion has no hydration shell.

We did not perform experiments with monomolybdates in solution at room temperature because we expect an even less perturbed spectrum than that of the polymolybdate in solution. Thus, it is practically impossible to differentiate between the two species in solution at room temperature. However, both species yield very different TDPAC spectra when immobilized, e.g., by shock-freezing to 77 K (*17*).

Solid APM was neutron irradiated and dissolved in H_2O. The solution was stirred for 1 h in order to remove all color centers and to achieve equilibrium. A concentration of 0.034 *M* APM (i.e., 0.24 *M* referring to monomeric MoO_4^{2-}) was selected to simulate the pore-filling impregnation conditions for the preparation of Al_2O_3-supported catalysts. We measured solutions in the regime $0 \leq$ pH ≤ 14 (*17*). The pH was adjusted by adding aliquots of NaOH or HCl, which had been determined previously in a titration experiment using solutions of nonirradiated APM so as to avoid

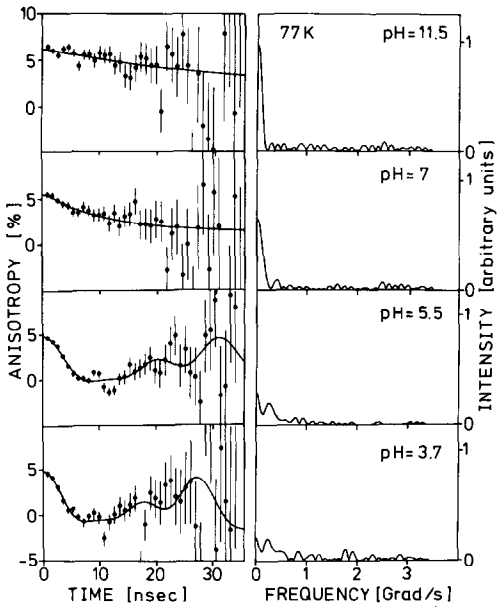

FIG. 13. TDPAC spectra (left) and their Fourier transforms (right) of frozen molybdate solutions at various pH values.

contamination of the pH electrodes. After equilibration, the samples were shock-frozen by immersion into liquid nitrogen. In Fig. 13 the TDPAC spectra and their Fourier transforms are shown for varying pH values. At pH $\geq$ 7 the anisotropy decreases only very slightly with time; i.e, the NQI is very small. This corresponds to the peak at $\omega = 0$ in the Fourier spectra. For values of pH < 7 the anisotropy decreases much faster, and characteristic peaks at higher frequencies build up, similar to those of crystalline APM. There is a further small change for pH < 2, where the average NQI decreases slightly.

Since MoO_4^{2-} in aqueous solution undergoes several polymerization and protonation reactions we should in principle not expect to have a single species in solution (*18*). Nevertheless we attempted to analyze the spectra with the following assumption: at pH > 6 the dominant species is MoO_4^{2-}; hence, we assumed an average frequency $\omega = 0$ for the undistorted tetrahedron but allowed for some frequency distribution since the solutions were rather concentrated. The mole fraction of this species and the width Γ were treated as free parameters. The other mole fraction is due to polymolybdates, and we kept the discrete frequency $\omega_1 = 229$ Mrad/s and the asymmetry parameter $\eta = 0.4$ fixed except where stated otherwise. These NQI parameters had been previously obtained from a very accurate measurement of a frozen solution at pH 5.5 (*19*). For pH 2.0, 2.7, and 3.7 it was necessary to increase ω by 30 to 70 Mrad/s. All results are summarized in Table 3. The onset of polymerization at pH $\approx$ 6 agrees with observations by Tytko and Glemser (*18*) for aqueous Na_2MoO_4 solutions and is clearly demonstrated in titration experiments, shown in Fig. 14. The plateau around pH 6, i.e., the buffer capacity, is larger for higher APM concentrations.

Summing up, as in the case of crystalline compounds, we have a vanishing or very low NQI for monomeric MoO_4^{2-} and interaction frequencies between 230 and 300 Mrad/s for polymolybdates in frozen solutions. This clear-cut distinction between monomeric and polymeric molybdates shown by the NQI suggests that it should be possible to apply the same technique to the characterization of adsorbates on Al_2O_3. This is discussed in the next section.

TABLE 3

Results of Least-Squares Fits of the Data Obtained for Frozen Molybdate Solutions[a]

pH	$\delta\omega$ (HWHM) for $\omega = 0$ (Mrad/s)	α (%)	ω_1 (Mrad/s)	η
14	17(4)	100	—	—
11.5	20(6)	100	—	—
9	50(13)	100	—	—
7	54(10)	95	229	0.40
5.5	0(13)	10	229	0.40
3.7	—	—	260	0.37
2.7	—	—	260	0.37
2.0	—	—	298(18)	0.44(8)
0	—	—	193(8)	0.20

[a] The quantities without quoted error limits were not treated as adjustable parameters.

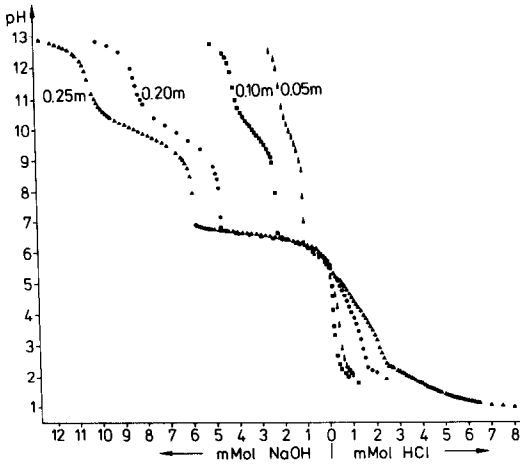

FIG. 14. Titration curves of aqueous molybdate solutions of varying concentrations.

3.3. *Molybdate Adsorption on Al_2O_3*

The first preparation step in Mo-based heterogeneous-supported catalysts is usually the impregnation of a suitable support having a high surface area with an APM solution (*20, 21*). We used Al_2O_3 PURAL SB from CONDEA with a BET surface area of about 150 m^2/g. In most cases this Al_2O_3 was calcined in air at 1023 K for 16 h prior to impregnation in order to eliminate adsorbed water. The APM solutions had a concentration of 0.034 *M* APM, corresponding to 0.24 *M* MoO_4^{2-}. We took, e.g., 105 mg APM, 570 μl H_2O, and 630 mg Al_2O_3, in order to produce a "theoretical monolayer coverage" with 12 wt% MoO_3, denoted by Mo12Al. Two procedures were followed: the "pore filling" or "incipient wetness" method and a modified version of the "equilibrium adsorption" method.

Pore filling method. Mo3Al, Mo6Al, Mo9Al, Mo12Al, and Mo15Al were studied. The different loadings were obtained using appropriate amounts of APM while keeping the amount of H_2O and Al_2O_3 constant. In this method there is no supernatant liquid. With this procedure, there is no way to perform pH measurements, e.g., of the solution in the pores. Moreover, it is difficult to determine the degree of adsorption. Here, TDPAC measurements are extremely valuable. In Fig. 15 Fourier transforms of TDPAC spectra for various oxidic precursors are shown both at 300 K (left) and at 77 K (right). At low concentrations, the TDPAC spectra are only weakly perturbed, whereas at higher concentrations the discrete frequency components gain intensity. This is clearly visible in the peak at $\omega = 0$ in the Fourier spectra, which is smallest for Mo12Al and increases slightly again for Mo15Al, i.e., beyond monolayer coverage. It is tempting to identify the unperturbed fraction α measured at 300 K with adsorbed MoO_4^{2-} and the perturbed fraction $(1 - \alpha)$ having discrete frequencies with adsorbed polymolybdates (*22*). This identification would be correct if the degree of adsorption were 100%. This, however, is not necessarily the case and the unperturbed

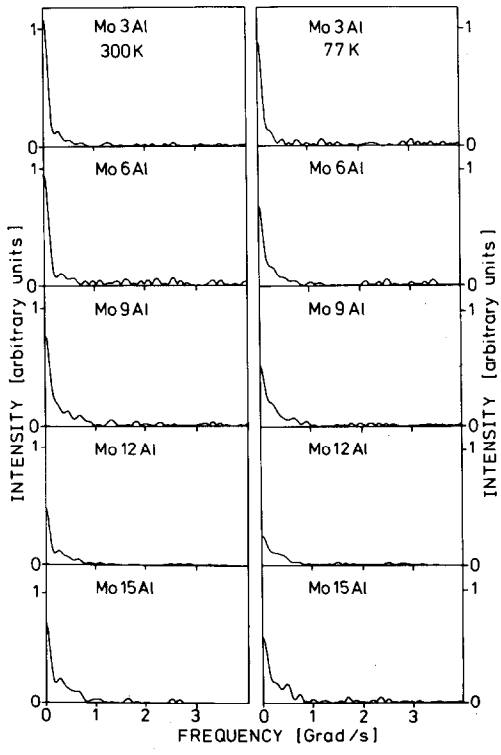

FIG. 15. Fourier transforms of TDPAC spectra of various Mo/Al_2O_3 oxide precursors taken at 300 K (left) and 77 K (right).

fraction at 300 K, i.e., α_{300}, might possibly include polymolybdates in solution (see Section 3.2): $\alpha_{300} = (MoO_4^{2-})_{adsorbed} + (polymolybdates)_{solution}$.

In a second experiment at 77 K, where the molecules in solution are immobilized, this second contribution would show up as a discrete frequency and hence the unperturbed fraction α_{77} decreases to the true adsorbed MoO_4^{2-} fraction: $\alpha_{77} = (MoO_4^{2-})_{adsorbed}$. From the difference in the two values we obtain the degree of adsorption P:

$$P = 1 - (\alpha_{77} - \alpha_{300}). \qquad (11)$$

The ratio of polymolybdates (poly) to adsorbed monomolybdates (mono) is given by (poly and mono both normalized to total molybdenum content)

$$\text{poly/mono} = \frac{\alpha_{300}}{1 - \alpha_{77}}. \qquad (12)$$

It can be easily shown that the neglect of a possible monomeric species in solution would lead to higher degrees of adsorption and to higher poly/mono ratios. Inspection of Fig. 15 shows that there is a further reduction of the $\omega = 0$ peak at 77 K compared to that at 300 K, which, however, is not dramatic (it should be mentioned that all measurements were performed under identical geometries with the samples being in identical sample holders inside the same Dewar, thus allowing direct quantitative comparisons). Hence, we can state at once that we always have a high degree of adsorption. The results obtained from least-squares fits are summarized in Table 4.

In this analysis the following parameters were kept constant: width of the frequency distribution centered around $\omega = 0$, $\Gamma = 20$ Mrad/s; frequency of the discrete component, $\omega_1 = 242$ Mrad/s; width of the frequency distribution of this component, $\delta_1\omega_1 = 12$ Mrad/s; asymmetry parameters, $\eta = 0.4$. In most cases an additional component with $\omega_2' = 700$ Mrad/s and $\delta_2'\omega_2' = 35\%$ ($\eta' = 0$) was found necessary to improve the fit quality (up to 30% population). This is attributed to defects produced during irradiation which persist after dissolution of APM (see section 3.1) and also after impregnation. This assignment is substantiated by the fact that colorless solutions did not require this additional component whereas "blue" precursors did, especially when the measurement at 77 K was carried out immediately after impregnation, thus preventing the decoloration.

We note that at low loadings monomeric MoO_4^{2-} is adsorbed preferentially while the opposite is true for loadings higher than 9 wt% MoO_3. This observation is consistent with previous Raman (*23–26*) and UV–Vis spectroscopic (*23, 24*) results. This can be understood as follows: the buffer capacity of the APM solution is small at low concentrations (Fig. 14) (*27*). Thus it is possible that the pH of the liquid in the pores is increased sufficiently in the course of the adsorption to allow substantial depolymerization at pH $\geq$ 7. Therefore MoO_4^{2-} is predominantly adsorbed. At higher concentrations, the pH shift is less significant, and we do not reach the pH for depolymerization. In this respect, it is not clear whether adsorbed polymolybdate can eventually be desorbed and depolymerized in the solution in the pores—provided that the pH is sufficiently high—and then be readsorbed as monomolybdates. A measurement with two Mo12Al samples at 300 K, however,

TABLE 4

Degree of Adsorption and Ratio of Adsorbed Polymolybdates to Adsorbed Monomolybdates for Various Coverages

System	Degree of adsorption (%)	$(\text{Poly/mono})_{ads}$
Mo3Al	100(3)	0.57(6)
Mo6Al	76(3)	0.95(18)
Mo9Al	95(2)	2.65(36)
Mo12Al	90(3)	4.29(1.22)
Mo15Al	100(3)	3.48(72)

yielded a constant α_{300} over a period of 3 days within better than 10% accuracy. This was found irrespective of the support pretreatment, i.e., freshly calcined or not. Hence, we do not expect subsequent equilibration to play an important role.

Equilibrium adsorption. We used the same solution as for the pore filling method but added only 40% of the Al_2O_3. Hence the solution excess was 2.5, which is low compared to the usual excess used in the equilibrium method (*23*). On the one hand we wanted to be as close as possible to the pore filling conditions (cf. buffer capacity of APM solutions (Fig. 14) (*27*)), and on the other hand we wanted to separate the supernatant liquid from the impregnated support with the possibility to determine the pH and to perform separate TDPAC measurements on both the solution and the solid.

We studied two loadings only: Mo3Al and Mo12Al. In addition, Mo12Al was studied whereby the supernatant solution was subsequently adjusted to pH 9. After equilibration the samples were centrifuged and the liquid was separated from the solid. For Mo3Al an equilibration time of 1 h was found sufficient, as indicated by the low γ-activity in the supernatant liquid. This was not true for Mo12Al. In this case, another measurement with an equilibration period of 18 h was performed.

The results for the solid Mo3Al, Mo12Al, and Mo12Al in basic solution as well as for the corresponding supernatant solutions (all spectra were taken at 77 K) are shown in Fig. 16. For Mo3Al the frozen solution shows monomolybdates only, i.e., complete depolymerization occurred during adsorption, whereas the solid exhibits a small amount of polymolybdates only. For Mo12Al and 1 h of equilibration, both the solid and the frozen solution exhibit essentially polymolybdates. This situation changes drastically after 18 h of equilibration. Now the frozen solution contains about 80% monomolybdates while the surface adsorbates are still essentially polymolybdates. This means that the depolymerization in the supernatant liquid is a slow process and requires several hours. Moreover, equilibration between the surface adsorbates and the solution via desorption/readsorption apparently plays no role.

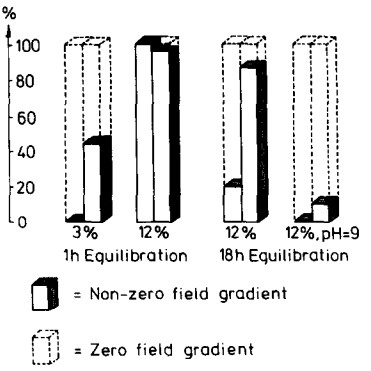

FIG. 16. Bar diagrams showing poly- and monomolybdate fractions of both the supernatant liquid (left bars) and the adsorbate (right bars) for Mo3Al (1-h equilibration), for Mo12Al (1-h and 18-h equilibration), and for Mo12Al in a solution at pH 9.

This invalidates all attempts to infer the surface adsorbate species from pH measurements of the supernatant solution. Recent ^{95}Mo NMR measurements of systems comparable to ours showed that the polymolybdate signal in solution is lost upon adsorption (*28*). The authors concluded that either all polymolybdates depolymerize upon adsorption or, alternatively, the adsorbate polymolybdate resonance is much too broad to be detectable. In order to distinguish between these possibilities, the authors then investigated the supernatant solution and found no polymolybdates. Hence, they concluded that there is no polymolybdate adsorbed either. The present results cast some doubt on this conclusion.

At pH 9 both the solid and the frozen solution exhibited essentially monomolybdates, as expected. As a byproduct we could estimate the degree of adsorption by measuring the γ-activities in the liquid and the solid. Whereas we had 70% of the activity on the Al_2O_3 support for Mo12Al, we

had only about 40% on the solid when the pH of the supernatant liquid was raised on purpose to pH 9. This tendency is to be expected in view of the isoelectric point of aluminas at pH 7–9 (*29*). Interestingly, the polymolybdate fractions qualitatively parallel the blue color of the samples, especially when immediately stored at 77 K. For example, with Mo3Al the liquid turns immediately colorless, whereas the solid decolorizes more slowly. With Mo12Al after 1 h of equilibration, both the liquid and the solid remain deep blue. The curious situation of the coexistence of predominantly monomolybdates in solution with predominantly polymolybdates on the surface is directly visible; the supernatant liquid has turned colorless after 18 h while the solid is still blue. Increasing the pH to 9 leads to immediate decoloration, as expected. Thus, the color of the impregnation solution serves as an interesting indicator in two respects: first, the color signals the presence of polymolybdates in solution and in the adsorbates; second, all speculations about monomeric adsorption with subsequent repolymerization (*24, 30*) can be ruled out at once because the blue color disappears upon depolymerization and would not reappear upon subsequent repolymerization. This indicator function apparently works because the color center in solid APM is rather stable when APM is dissolved in water and even when the heptamolybdate is adsorbed onto Al_2O_3.

Finally, it should be mentioned that the equilibrium adsorption technique seems to yield better defined surface adsorbate species. This is shown in Fig. 17, top, for Mo12Al at 300 K after 18 h of equilibration. This spectrum was fitted with a fraction of 35% with a frequency distribution around $\omega = 0$ and a width $\Gamma = 70$ Mrad/s, while the majority had $\omega_1 = 251(4)$ Mrad/s and $\eta = 0.35(2)$ with $\delta\omega_1 = 5$ Mrad/s, the latter being almost negligible and much smaller than all values obtained by the pore filling method (even smaller than that obtained for solid APM). The NQI parameters are only

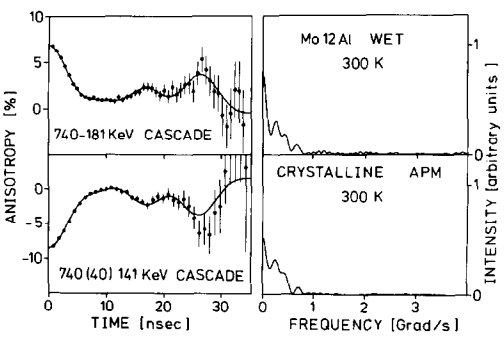

FIG. 17. TDPAC and Fourier spectra obtained for Mo12Al prepared by equilibrium adsorption for 18 h (top) and TDPAC spectrum of APM at 300 K taken after dissolution in water and precipitation with ethanol (bottom).

slightly shifted compared to the value for solid APM (Fig. 17, bottom). Therefore, and because of the persistence of the color center upon adsorption, we can safely conclude that the adsorbed species are heptamolybdates. This rules out the concept of a homogeneous monolayer coverage (*31*); it rather suggests islands of heptamolybdates and uncovered support surfaces. These observations are in good agreement with conclusions drawn from Raman spectra of impregnated Mo/Al_2O_3 catalysts in the wet state (*23, 25*).

3.4. Drying, Calcination, and Postimpregnation

Our studies of dried, calcined, and postimpregnated precursors are less extensive than our impregnation studies (*22*). Upon drying the wet precursor Mo12Al at 393 K for 2 h (obtained by the pore filling method) we measured the TDPAC spectrum at 77 K (Fig. 18a). Compared to the spectrum of the sample before drying (cf. Fig. 15) there is very little change. Moreover, in samples which were colored and exhibited a high-frequency component, this defect signal persisted after drying. Hence, apart from partially removing water in the pores, we still have basically the same surface species.

A spectrum taken at 300 K after calcina-

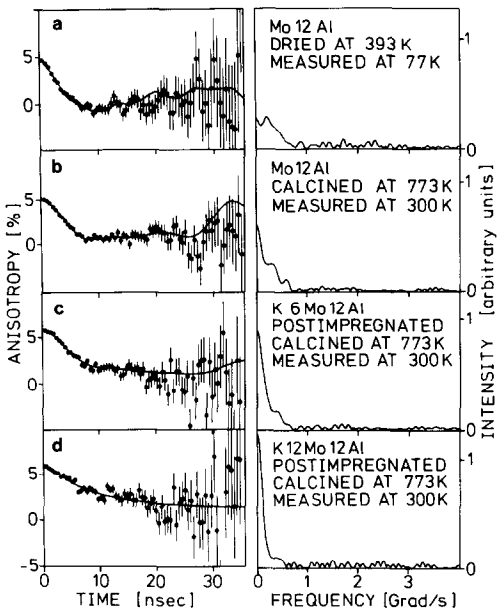

FIG. 18. (a) TDPAC and Fourier spectra of Mo12Al taken at 77 K after drying the wet precursor for 2 h at 393 K. (b) TDPAC spectrum of Mo12Al taken at 300 K after calcination at 773 K for 2 h. (c) TDPAC spectrum of K6Mo12Al taken at 300 K (Mo12Al postimpregnated with K_2CO_3). (d) TDPAC spectrum of K12Mo12Al taken at 300 K.

tion at 773 K for 2 h is shown in Fig. 18b. Now, all high-frequency components disappeared; i.e., all defects are annealed. The fitted theoretical function consisted of a fraction of 83(1)% with $\omega_1 = 197$ Mrad/s and $\eta = 0.21$, the remainder had $\omega = 0$. This increase of the component with $\omega = 0$ suggests that partial decondensation of polymolybdates. When the calcination was performed at 873 K, this $\omega = 0$ fraction increased even further. Beginning formation of $Al_2(MoO_4)_3$ under these conditions cannot be excluded.

The majority species after typical calcination procedures at 773 K is still the heptamolybdate in full accordance with structural information from Raman spectroscopy (*23, 26, 32*). It must also be concluded that even after calcination homogeneous monolayers are not formed; rather, molybdate islands still persist, as has been indicated by ion-scattering spectroscopy (*33–35*).

Upon postimpregnation of calcined Mo12Al with aqueous K_2CO_3 solutions (atomic ratio K : Mo = 0.4 and 0.8, corresponding to K6Mo12Al and K12Mo12Al, respectively), we observed a dramatic change of the TDPAC spectra (Figs. 18c and 18d). For K6Mo12Al a fraction of 58% exhibited $\omega = 0$ with a width of $\Gamma = 58$ Mrad/s, whereas for K12Mo12Al this fraction increased to 82(2)%. The remainder had a discrete frequency of $\omega = 186(7)$ and 380 Mrad/s, respectively, the latter being unusually high and still unidentified. This result shows that the postimpregnation with K_2CO_3 leads to almost complete decondensation of the polymolybdates, provided that the K : Mo ratio is sufficiently high. This observation is in good agreement with results for a $NiMo/Al_2O_3$ catalyst on the basis of Raman and optical spectroscopy (*36*) and clearly demonstrates that the adsorption of the heptamolybdate is not sufficiently strong to prevent subsequent decondensation.

4. SUMMARY

By measuring the NQI of $^{99}Mo \rightarrow {}^{99}Tc$ by TDPAC we have attempted to answer the long-standing question: What is the adsorbed species when Al_2O_3 is impregnated with APM solutions? *At sufficiently high coverages polymolybdates are adsorbed predominantly.* Moreover, it has been found treacherous to infer the adsorbed species from an investigation of the supernatant liquid in equilibrium adsorption studies.

TDPAC is very well suited to *in situ* studies. Therefore, we are currently investigating the reduction and sulfidation processes of the oxidic precursors. In addition, we are studying highly dispersed MoS_2 derived from thermal decomposition of $(NH_4)_2MoS_4$ and from Mo_3S_{13} clusters. Neither the adsorbed sulfide nor the unsupported sulfides correspond to bulk MoS_2. Finally, first ex-

periments monitoring the catalyst during thiophene conversion *in situ* are under way.

ACKNOWLEDGMENTS

This work was supported by the Deutsche Forschungsgemeinschaft and the Bundesministerium für Forschung und Technologie, FRG. We thank Professor G. M. Kalvius for his continuous interest in this work and for his hospitality.

REFERENCES

1. Gates, B. C., Katzer, J. R., and Schuit, G. C. A., "Chemistry of Catalytic Processes," McGraw–Hill, New York, 1979.
2. Ledoux, M. J., *in* "Catalysis," p. 125. Specialist Periodical Reports, The Royal Society of Chemistry, London, 1985.
3. Wilhelm, F. C., Tsigdinos, C. A., and Ferenc, R. A., *in* "Proceedings, Climax 3rd Intern. Conf. on Chemistry and Uses of Molybdenum" (H. F. Barry and P. C. H. Mitchell, Eds.), p. 219. Climax Molybdenum Co., Ann Arbor, MI, 1979.
4. Murchison, C. B., *in* "Proceedings, Climax 4th Intern. Conf. on Chemistry and Uses of Molybdenum" (H. F. Barry and P. C. H. Mitchell, Eds.), p. 197. Climax Molybdenum Co., Ann Arbor, MI, 1982.
5. Aldrige, C. L., and Kalina, T., U.S. Patent 3,850,840 (1974); Segura, M., Aldrige, C. L., Riley, K. L., and Pine, L. A., U.S. Patent 3,974,096 (1976).
6. Steffen, R. M., and Frauenfelder, H., *in* "Alpha-, Beta-, Gamma-Ray-Spectroscopy (K. Siegbahn, Ed.), Vol. 2, p. 997. North-Holland, Amsterdam, 1965.
7. Frauenfelder, H., and Steffen, R. M., *in* "Perturbed Angular Correlations" (E. Karlsson, E. Matthias, and K. Siegbahn, Eds.), p. 1. North-Holland, Amsterdam, 1964.
8. Lerf, A., and Butz, T., *Angew. Chem. Int. Ed. Engl.* **26,** 110 (1987).
9. Lederer, C. M., and Shirley, V. S. (Eds.), "Table of Isotopes," 7th ed. Wiley, New York, 1978.
10. Singh, K., and Sahota, H. S., *J. Phys. Soc. Japan* **51,** 3766 (1982).
11. Ni, X., Sun, G., Butz, T., and Lerf, A., *Chem. Phys.* **123,** 455 (1988).
12. Rogers, J. D., and Vasquez, A., *Nucl. Instrum. Methods* **130,** 539 (1975).
13. Kuo, F. F., and Kaiser, J. F., "System Analysis by Digital Computer," Wiley, New York, 1966.
14. Butz, T., Lerf, A., Vogdt, C., and Eid, A. M. M., *Hyperfine Interact.* **15/16,** 915 (1983).
15. Vogdt, C., Butz, T., Lerf, A., and Knözinger, H., *Polyhedron* **5,** 95 (1986).
16. "Gmelin Handbook of Inorganic Chemistry, Mo Supplement" (K. H. Tytko, Ed.), Vol. B4. Verlag Chemie, Weinheim, 1985.
17. Lerf, A., Vogdt, C., Butz, T., Eid, A. M. M., and Knözinger, H., *Hyperfine Interact.* **15/16,** 921 (1983).
18. Tytko, K. H., and Glemser, O., *Adv. Inorg. Chem. Radiochem.* **19,** 239 (1976); Tytko, K. H., Baethe, G., Hirschfeld, E. R., Mehmke, K., and Stellhorn, D., *Z. Anorg. Allg. Chem.* **503,** 43 (1983).
19. Vogdt, C., Thesis, University of Munich, 1987.
20. Hall, W. K., *in* "Proceedings, Climax 4th Intern. Conf. on Chemistry and Uses of Molybdenum" (H. F. Barry and P. C. H. Mitchell, Eds.), p. 224. Climax Molybdenum Co., Ann Arbor, MI, 1982.
21. Knözinger, H., *in* "Catalysis by Acids and Bases" (B. Imelik *et al.,* Eds.), p. 111. Elsevier, Amsterdam, 1985.
22. Vogdt, C., Butz, T., Lerf, A., and Knözinger, H., *in* "Proceedings, 8th International Congress on Catalysis, Berlin, 1984," Vol. 3, p. 117. Dechema, Frankfurt-am-Main, 1984.
23. Wang, L., and Hall, W. K., *J. Catal.* **77,** 232 (1982).
24. Jeziorowski, H., and Knözinger, H., *J. Phys. Chem.* **83,** 1166 (1979).
25. Kasztelan, S., Payen, E., Toulhoat, H., Grimblot, J., and Bonnelle, J. P., *Polyhedron* **5,** 157 (1986).
26. Payen, E., Grimblot, J., and Kasztelan, S., *J. Phys. Chem.* **91,** 6642 (1987).
27. Sasaki, Y., and Sillen, L. G., *Acta Chem. Scand.* **18,** 1014 (1964); *Arkiv. Kemi* **29,** 253 (1968).
28. Luthra, W. P., and Cheng, W. C., *J. Catal.* **107,** 154 (1987).
29. Parks, G. C., *Chem. Rev.* **65,** 177 (1965).
30. Medema, J., van Stam, C., de Beer, V. H. J., Konings, A. J. A., and Koningsberger, D. C., *J. Catal.* **53,** 386 (1978).
31. Sonnemans, J., and Mars, P., *J. Catal.* **31,** 209 (1973).
32. Leyrer, J., Vielhaber, B., Zaki, M. I., Zhuang, S., Weitkamp, J., and Knözinger, H., *Mater. Chem. Phys.* **13,** 301 (1985).
33. Houalla, M., Kibby, C. L., Leonidas, P., and Hercules, D. M., *J. Catal.* **83,** 50 (1983).
34. Houalla, M., Kibby, C. L., Eddy, E. L., Petrakis, L., and Hercules, D. M., *in* "Proceedings, 8th International Congress on Catalysis, Berlin, 1984," Vol. 4, p. 415. Dechema, Frankfurt-am-Main, 1984.
35. Kasztelan, S., Grimblot, J., and Bonnelle, J.-P., *J. Phys. Chem.* **91,** 1503 (1987).
36. Kantschewa, M., Delannay, F., Jeziorowski, H., Delgado, E., Eder, S., Ertl, G., and Knözinger, H., *J. Catal.* **87,** 482 (1984).